15

Electron beam diagnostics using hard X-rays at the SRF „SKIF“

© Yu.V. Khomyakov,[1,2] O.I. Meshkov,[2] V.P. Nazmov,[2,5] Ya.V. Rakshun,[2,3] V.A. Chernov,[2] N.I. Chkhalo[4]

[1] SRF „SKIF“,
630559 Koltsovo, Novosibirsk region, Russia
[2] Budker Institute of Nuclear Physics, Siberian Branch of the Russian Academy of Sciences,
630090 Novosibirsk, Russia
[3] Sobolev Institute of Geology and Mineralogy, Siberian Branch Russian Academy of Sciences,
630090 Novosibirsk, Russia
[4] Institute of Physics of Microstructures, Russian Academy of Sciences,
603950 Nizhny Novgorod, Russia
[5] Institute of Solid State Chemistry and Mechanochemistry, Siberian Branch, Russian Academy of Sciences,
630090 Novosibirsk, Russia
e-mail: yu.v.khomyakov@yandex.ru

Received June 5, 2025
Revised June 5, 2025
Accepted June 5, 2025

This paper briefly describes some methods for measuring ultra-low emittance of an electron beam using hard X-rays. It is shown that a combination of diagnostic methods eliminates the influence of errors introduced by individual X-ray optical components. Modeling of radiation beams has been performed in accordance with the proposed schemes for measuring emittance. For the most conservative scheme, a pinhole camera, achievable resolution is estimated to be 3.7 μm. An optical design for a specialized diagnostic beamline of the SRF „SKIF“has been proposed.

Keywords: synchrotron radiation, hard X-rays, electron emittance, pinhole, speckle pattern, Billet lens, Young experiment, Young interferometer, Billet interferometer, pinhole camera, Kirkpatrick–Baez mirrors.

DOI: 10.61011/TP.2025.10.62088.140-25

Introduction

Beam emittance ε_e, i.e. a phase volume occupied by an electron beam in the position–angle space, is the key property of synchrotron radiation (SR) sources because it is this property that defines the brightness of generated radiation. Due to the growth of acceleration technology, in particular, to transition to Multi-Bend Achromat type magnetic cells, new fourth-generation SR sources such as the SRF „SKIF“ [1] have a design horizontal beam emittance $\varepsilon_{e,x}$ reduced to approximately 100 pm·rad. Fourth-generation SR sources are diffraction-limited up to a soft X-ray range ($E^*_{ph} \sim 1$ keV), while the third-generation and second-generation sources are diffraction-limited up to ultraviolet and infrared ranges, respectively [2]. Diffraction limitation of a source displays itself in the fact that beamlines using SR with the photon energy $E_{ph} < E^*_{ph}$ virtually don't gain in brightness from further reduction of the electron beam emittance.

Beam emittance diagnostics comes down to measuring the electron beam cross-section ($\sigma_e \sim 10\,\mu$m), for which modern machines more often use hard X-ray SR. The most common approach involves source imaging using a camera obscura [3,4] or more sophisticated imaging X-ray optical systems [5–8]. The achievable resolution in this case is limited by the SR directional pattern width that defines the maximum numerical aperture of imaging optics. Interferometric measurements where coherent properties of SR are investigated for beam dimension recovery serve as an alternative. As an X-ray interferometer, a pair of slits [9] or a pair of pinholes [10] is used in the simplest case, and a pair of diffraction gratings is used in a more complex case [11]. Heterodyne interferometry based on the near-field speckle pattern analysis is developing rapidly [12,13]. The achievable resolution of interferometric techniques is fundamentally limited only by a chosen wavelength. Special focus shall be made on π-polarization and obstacle diffractometry that are used in the ultraviolet range and make it possible to examine micron-size electron beams [14]. Nevertheless, for measurement interpretation, these methods require rigorous numerical simulation of radiation generation process and diffraction effects, and therefore are not direct ones.

Direct electron beam diagnostics techniques using SR demonstrate a successive transition to a more short-wave radiation: from visible light at second-generation facilities to ultraviolet and X-rays at third-generation and fourth-generation facilities. This transition is caused by more stringent resolution requirements for measurement techniques and a shift of the source diffraction limitation range edge E^*_{ph} towards higher photon energies. Otherwise, direct precision beam emittance measurements of new SR sources are impossible without X-ray diagnostic systems.

This work summarizes some variations of the above-mentioned ultra-low beam emittance measurement tech-

niques and proposes an optical design for a specialized hard X-ray diagnostic beamline of the SRF „SKIF“İt is proposed to combine diagnostic techniques for cross-checking measurement results and eliminating the influence of individual X-ray optical components.

1. Emittance measurement techniques

Electron beam cross-section dimensions at the emission point are related to the horizontal and vertical emittances $\varepsilon_{e,x|y}$, relative energy spread σ_E/E, dispersion and betatron functions η_x and $\beta_{x|y}$ (usually $\eta_y = 0$) [15]:

$$\sigma_{e,x} = \sqrt{\varepsilon_{e,x}\beta_x + \left(\eta_x \frac{\sigma_E}{E}\right)^2},$$

$$\sigma_{e,y} = \sqrt{\varepsilon_{e,y}\beta_y}. \quad (1)$$

With known σ_E/E, η_x and $\beta_{x|y}$, the emittance measurement problem is reduced to beam cross-section measurement.

For fourth-generation SR sources, typical emittances are $\varepsilon_{e,x} \sim 100\,\text{pm·rad}$ and $\varepsilon_{e,y} \sim 10\,\text{pm·rad}$ [16,17]. The beam has typical sizes $\sigma_{e,x} \sim \sigma_{e,y} \sim 10\,\mu\text{m}$ and divergences $\sigma'_{e,x} \sim 10\sigma'_{e,y} \sim 10\,\mu\text{rad}$, i.e.

$$\varepsilon_{e,x} = \sigma_{e,x} \cdot \sigma'_{e,x} \sim 10\,\mu\text{m} \cdot 10\,\mu\text{rad} = 100\,\text{pm·rad},$$

$$\varepsilon_{e,y} = \sigma_{e,y} \cdot \sigma'_{e,y} \sim 10\,\mu\text{m} \cdot 1\,\mu\text{rad} = 10\,\text{pm·rad}. \quad (2)$$

Limitations of $\sigma_{e,x|y}$ measurement accuracy are associated with orbit curvature at the point of SR emission, angular aperture of SR detection and light wave properties [18].

Radiation emitted by one electron has intrinsic non-zero emittance ε_r, that may be evaluated from the uncertainty relation [2]:

$$\varepsilon_r = \sigma_r \cdot \sigma'_r \sim \frac{\lambda}{4\pi} = \frac{98.7}{E_{ph}[\text{keV}]}\,\text{pm·rad}, \quad (3)$$

where σ_r is the effective size of a source formed by one electron at zero beam emittance, σ'_r is the divergence of radiation emitted by one electron, λ is the SR wavelength. A source is referred to as a diffraction-limited source for radiation with a quantum energy lower than the threshold value $E_{ph} < E^*_{ph}$, i.e. when $\varepsilon_{e,x} < \varepsilon_r$. E^*_{ph} and the corresponding wavelength λ^* at the SRF „SKIF“ are

$$\lambda^* = 4\pi\varepsilon_{e,x} \sim 1\,\text{nm},$$

$$E^*_{ph} = \frac{\hbar c}{\lambda^*} \sim 1\,\text{keV}. \quad (4)$$

SR is characterized by the directional pattern with $\sigma'_r \sim 1/\gamma \ll 1$ (for machines with an electron energy of 3 GeV, the Lorentz factor $\gamma \approx 6000$). Due to the uncertainty of the transverse coordinate of the point of photon emission by an electron (i.e. due to a finite value of σ_r), it is fundamentally impossible to measure beam cross-section dimensions directly using SR at $E_{ph} \ll E^*_{ph}$ by any techniques, including interferometric ones. Evaluating the effect for E^*_{ph} according to (3), we have:

$$\sigma_r \sim \frac{\lambda}{4\pi\sigma'_r}\Big|_{\lambda=\lambda^*} \sim \left(\frac{1}{\gamma}\right)^{-1}\varepsilon_{e,x}$$

$$\sim 6000\,\text{rad}^{-1} \cdot 100\,\text{pm·rad} = 0.6\,\mu\text{m} \sim \frac{\sigma_{e,x|y}}{10}. \quad (5)$$

Even more stringent restriction occurs when measuring beam dimensions by source imaging because the maximum effective numerical aperture (NA) of imaging optics is limited by the SR divergence: $\text{NA} \sim \sigma'_r \sim 1/\gamma$. Resolution of such system σ in the ideal case corresponds to the Abbe limit:

$$\sigma = \frac{\lambda}{2\text{NA}}\Big|_{\lambda=\lambda^*} = 2\pi\varepsilon_{e,x}\gamma \sim 4\,\mu\text{m} \sim \sigma_{e,x|y}. \quad (6)$$

Note that the SR capture angle smallness neutralizes the effective source size broadening related to the beam orbit curvature.

At fourth-generation facilities one can overcome beam emittance measurement accuracy limitations (5) and (6) by reducing the wavelength, i.e. by transition to the hard X-ray range to $E_{ph} \gg E^*_{ph}$.

Any beam emittance measurement experiments using SR employ the effective source size $\sigma_{source,x|y}$ as a measured quantity. Assuming that different electrons in a bunch radiate incoherently in the hard X-ray range (i.e. the resulting far-field radiation intensity is the sum of radiation intensities of individual electrons), the source may be represented in the form of a convolution of the electron beam profile and effective single-electron source profile. Similarly, the observed $\sigma'_{source,x|y}$ to the same approximation is the result of electron beam and single electron radiation convolution. If an electron beam and a beam of photons emitted by one electron are assumed as Gaussian beams, then

$$\sigma^2_{source,x|y} = \sigma^2_{e,x|y} + \sigma^2_r,$$

$$(\sigma'_{source,x|y})^2 = (\sigma'_{e,x|y})^2 + (\sigma'_r)^2. \quad (7)$$

It follows from (5) that the contribution of σ_r remains considerable up to E^*_{ph}, and therefore it shall be considered in the moderate hard X-ray measurements. $\sigma_{e,x|y}$ and $\sigma'_{e,x|y}$ may be evaluated by deconvoluting the measured source profile using the a priori knowledge of the Twiss parameters of a storage ring. A more stringent approach to measurement post-processing includes the consideration of partial coherence effects that may be implemented by numerical simulation of stochastic emission of radiation by an electron bunch, for example, using Serval code [19].

Measurements of $\sigma_{source,x|y}$ that pose the major difficulty when determining the beam emittance are directly discussed in this section. Two main families of hard range techniques may be distinguished: source imaging and interferometry.

Source imaging at diagnostic beamlines is generally implemented using a camera obscura. Such measurements often use a rectangular pinhole with the side $A \sim 10\,\mu\text{m}$

formed by a pair of crossed slits made from a highly absorbing material. Pinhole size shall be chosen larger than SR transverse coherence lengths, but smaller than the source size [20], which is not always possible. Pinhole is placed as close as possible to the emission point at a distance of $p \sim 10\,\text{m}$ and the M-fold magnified source image is recorded using a two-axis detector spaced at $q = Mp$ from the pinhole. The use of a pinhole provides an infinite depth of field, but results in low light transmission of the system. Camera obscura resolution may be described using a point spread function (PSF). The detected image is a convolution of the magnified source profile with pinhole PSF and detector PSF. PSF of a square pinhole with the side A may be factorized, $\text{PSF}_{pinhole} = \text{PSF}_{pinhole,x}\text{PSF}_{pinhole,y}$, with „1D“ PSF expressed analytically [20,21]:

$$\text{PSF}_{pinhole,x|y}(\Omega, t) = \int_{-1}^{1} \frac{\sin[2(\xi\Omega + t\sqrt{\Omega})(1 - |\xi|)]}{\xi\Omega + t\sqrt{\Omega}}\, d\xi, \tag{8}$$

where ξ is the transverse coordinate normalized to the aperture size,

$$\Omega = \frac{2\pi(A/2)^2}{\lambda z},\ z = \frac{pq}{p+q},\ t = \frac{x|y}{\sqrt{\frac{\lambda}{2\pi z}}q}.$$

Pinhole PSF width $\sigma_{pinhole}$ is defined by a dimensionless parameter Ω. In [20,21], it is proposed to choose $\Omega = 4.5$ to minimize $\sigma_{pinhole}$, providing an optimum pinhole size condition:

$$(A/2)^2 \approx \frac{4.5\lambda z}{2\pi}. \tag{9}$$

Pinhole far-field resolution is

$$\sigma_{pinhole} \approx 0.64\sqrt{\frac{\lambda}{2\pi z}}\, q. \tag{10}$$

Assuming for the purpose of evaluation that the source and PSF of all imaging system components are Gaussian, rms size of the detected image σ_{image} may be given as [22]:

$$\begin{aligned}\sigma_{image}^2 &= M^2\sigma_{source}^2 + \sigma_{\text{PSF}}^2 \\ &= M^2\sigma_{source}^2 + \sigma_{pinhole}^2 + \sigma_{detector}^2.\end{aligned} \tag{11}$$

In real practice, $\sigma_{pinhole}/M \sim 6\,\mu\text{m}$ may be achieved in the hard X-ray range [3]. For fourth-generation SR sources, it turns out that $\sigma_{source,\,x|y} \sim \sigma_{pinhole} \sim \sigma_{detector}$, therefore recovery of true transverse dimensions of an electron bunch for source imaging using a camera obscura requires accurate simulation of pinhole PSF, detector PSF measurement and subsequent deconvolution of the detected intensity distribution.

Refractive, reflective, or diffractive optics may be used instead of the pinhole to provide a considerable gain in aperture ratio and reduce a exposure time per frame, however, at the same time it requires focusing on the source and, in some cases, the use of a monochromator.

Suppose source imaging uses focusing X-ray optics with a square aperture with side A. Such aperture corresponds, for example, to a crossed planar compound refractive lens [23,24] or a pair of Kirkpatrick-Baez (KB) mirrors [25]. For this optics, $A \sim 1\,\text{mm}$ is available, which is two orders of magnitude larger than the pinhole aperture, due to which diffraction blurring of the image may be neglected. Nevertheless, source transverse dimension measurements using focusing optics shall consider geometrical and chromatic aberrations limiting the ultimate resolution of the imaging system, see Section 3.

Interferometric measurements of SR coherent properties may use various optical setups: double-slit interferometer [9], Billet split lens [26], Lloyd mirror [27], Talbot interferometer [11], etc.

Let's consider a typical source dimension measurement setup in Young's experiment. After preliminary monochromatization, the SR beam passes through a pair of slits with a width a spaced apart at d and placed at a distance p from the emission point. A detector that records the interference pattern $I(x)$is placed at a distance $q \gg a, d$ from the slits:

$$I = 2I_0\,\text{sinc}^2\Big(\frac{\pi a}{\lambda q}x\Big)\Big[1 + \gamma_{coh}\cos\Big(\frac{2\pi d}{\lambda q}x\Big)\Big], \tag{12}$$

where γ_{coh} is the complex degree of coherence. In the hard X-ray range, the Van Cittert-Zernike theorem is valid [28], according to which γ_{coh} at a distance from an incoherent source may be expressed as the Fourier transform of the source intensity distribution. For the Gaussian source, we have

$$V = |\gamma_{coh}| = \exp\Big[-2\Big(\frac{\pi\sigma_{source}d}{\lambda p}\Big)^2\Big]. \tag{13}$$

V is the interferometric visibility:

$$V = \frac{I_{\max} - I_{\min}}{I_{\max} + I_{\min}}, \tag{14}$$

where $I_{\max}$ and $I_{\min}$ are the maximum and minimum intensities at the detector. V is determined by fitting the measured interference pattern (12). The source size is given from (13):

$$\sigma_{source} = \frac{\lambda p}{\pi d}\sqrt{\frac{1}{2}\ln\frac{1}{V}}. \tag{15}$$

Relative resolution of the double-slit interferometer can be derived from (15) [22] as

$$\frac{d\sigma_{source}}{\sigma_{source}} = \frac{dV}{12\ln(1/V)}. \tag{16}$$

The optimum visibility $V_0 = 0.368$ is derived from minimization of $d\sigma_{source}/\sigma_{source}$ with the fixed accuracy of dV. This yields the relation between the expected source size and the combination of optimum values of λ_0, p_0 and d_0:

$$\sigma_{source} = \frac{0.255\lambda_0 p_0}{d_0}. \tag{17}$$

To determine σ_{source} in real practice, the relation V and slit spacing are investigated by searching through a set of slit pairs with different d. Slit widths a are set small enough to meet the Fraunhofer diffraction approximation condition. Study [22] suggests selecting $a = d/5$. The width of interferometric envelope function (12) is sufficiently large to accommodate ~ 10 interference peaks. Actually, when measuring the electron beam dimensions in the double-slit experiment, the detector PSF width is the main limitation. $1\,\mu$m resolution was achieved in the visible range for such measurements [29]. Nevertheless, the method can be also implemented in the hard X-ray range [9].

Transition from the double-slit configuration to the Billet split lens [26] provides a gain in light transmission proportional to the lens and slit aperture ratio. The split lens forms a pair of mutually coherent secondary sources, for which the foregoing judgements concerning a pair of slits are valid. Interference pattern recording allows recovery of sizes of these secondary sources that in turn are related to the real source size by the reproduction ratio of the split lens. For electron beam information preservation, it is important that the split lens focus be not diffraction-limited.

As the SR source brightness increases, an X-ray heterodyne interferometry technique becomes available for electron beam cross-section measurements. This technique requires a minimum set of optics: monochromator and speckle pattern generator [12,13]. Abrasive paper or better a low absorbing porous acetylcellulose membrane may serve as the latter [12,30]. The speckle pattern generator is placed downstream of the monochromator at $p \sim 10-100$ m from the source and $q \sim 1$ m from the two-axis detector that records speckle patterns. Intensity distribution across the detector $I(x, y)$ and the normalized effective signal $I_n(x, y)$ are expressed as:

$$I(x, y) = |E_i|^2 + E_i^* E_s + E_s^* E_i + |E_s|^2 \simeq I_i + 2\mathrm{Re}(E_i^* E_s),$$

$$I_n(x, y) = \frac{I - I_i}{I_i}, \tag{18}$$

where E_i and E_s are the incident and scattered wave fields, respectively, $|E_i|^2 = I_i$, $|E_s| \ll |E_i|$. In the Fresnel diffraction mode, the power spectral density (PSD) of signal I_n may be factorized as follows [12,31]:

$$I_n(\xi) = T_{near-field}(\xi) I_{membrane}(\xi), \tag{19}$$

where $T_{near-field}(\xi)$ is the near-field optical transfer function, $I_{membrane}(\xi)$ is the Fourier transform of the speckle pattern generator (membrane) electron density. It is important that the spatial frequency range $(\xi_{\min}, \xi_{\max})$ is limited: $\xi_{\min}$ is defined by optics stability and $\xi_{\max}$ is defined by the detector PSF width. $T_{near-field}(\xi)$ in the specified range $(\xi_{\min}, \xi_{\max})$ is also factorized [12,31]:

$$T_{near-field}(\xi) = T_{Talbot}(\xi) T_{coherence}(\xi) \mathrm{FR}_{detector}(\xi), \tag{20}$$

where $\mathrm{FR}_{detector}$ is the detector response function (to be determined experimentally). T_{Talbot} and $T_{coherence}$ describe the Talbot effect and the influence of partial SR coherence, respectively:

$$T_{Talbot}(\xi) = \sin^2\left(\frac{\xi^2 q}{2k}\right), \tag{21}$$

$$T_{coherence}(\xi) = \exp\left[-\left(\frac{x^2}{{l_{coh,x}}^2} + \frac{y^2}{{l_{coh,y}}^2}\right)\right], \tag{22}$$

where $l_{coh,x|y}$ are the rms spatial coherence lengths. Expression (22) follows from the Van Cittert-Zernike theorem on the Gaussian source profile assumption. The spatial coherence lengths are related to the Gaussian source size as follows [2]:

$$l_{coh,x|y} = \frac{\lambda p}{3.545 \sigma_{source,x|y}}. \tag{23}$$

Thus, the near-field speckle pattern contains the beam size information in two coordinates at once. The technique resolution is defined by the detector in real practice.

2. Hard X-ray emittance measurement setup

For beam emittance measurements, the SRF „SKIF“ will use the „X-Ray Beam Diagnostics“ and „Hard X-Ray Metrology“ beamlines (Figure 1). Both beamlines will use „strong“ bending magnets with a field $B = 2.05$ T and corresponding SR critical energy $E_{ph,c} \approx 12$ keV as a radiation source. The frontends of beamlines will perform spectral filtration and primary SR beam collimation.

The „X-Ray Beam Diagnostics“ beamline is designed for continuous electron beam monitoring by hard X-ray source imaging. For this, the initial storage ring commissioning stages will use a square pinhole at $E_{ph} \sim 60-100$ keV placed 8 m from the source. The pinhole will consist of a pair of crossed adjustable precision slits made from cemented tungsten carbide. A molybdenum filter will be used to suppress the low-energy portion of the spectrum. The source image will be recorded using the 2D X-ray detector consisting of a thin scintillator with high effective atomic number (or example, BGO or LYSO), plane mirror, $\sim$ 10-fold magnification lens and CCD matrix. The detector will be placed 78 m from the source, i.e. at the experimental room end.

After achievement of the design beam emittance, a series of experiments is planned to study the behavior of an electron beam with high spatial and time resolution. For this purpose, the pinhole and molybdenum filter at the „X-Ray Beam Diagnostics“ beamline will be removed from the SR beam and a high-light-transmission achromatic KB mirror system, located 27m from the source, will be used for imaging. The KB system consists of two elliptical total external reflection (TER) mirrors operating in the $E_{ph} \sim 10-30$ keV band. A diamond filter will be used to suppress the low-energy portion of the spectrum. Note that the KB mirror system shall be preliminary characterized at a metrology beamline.

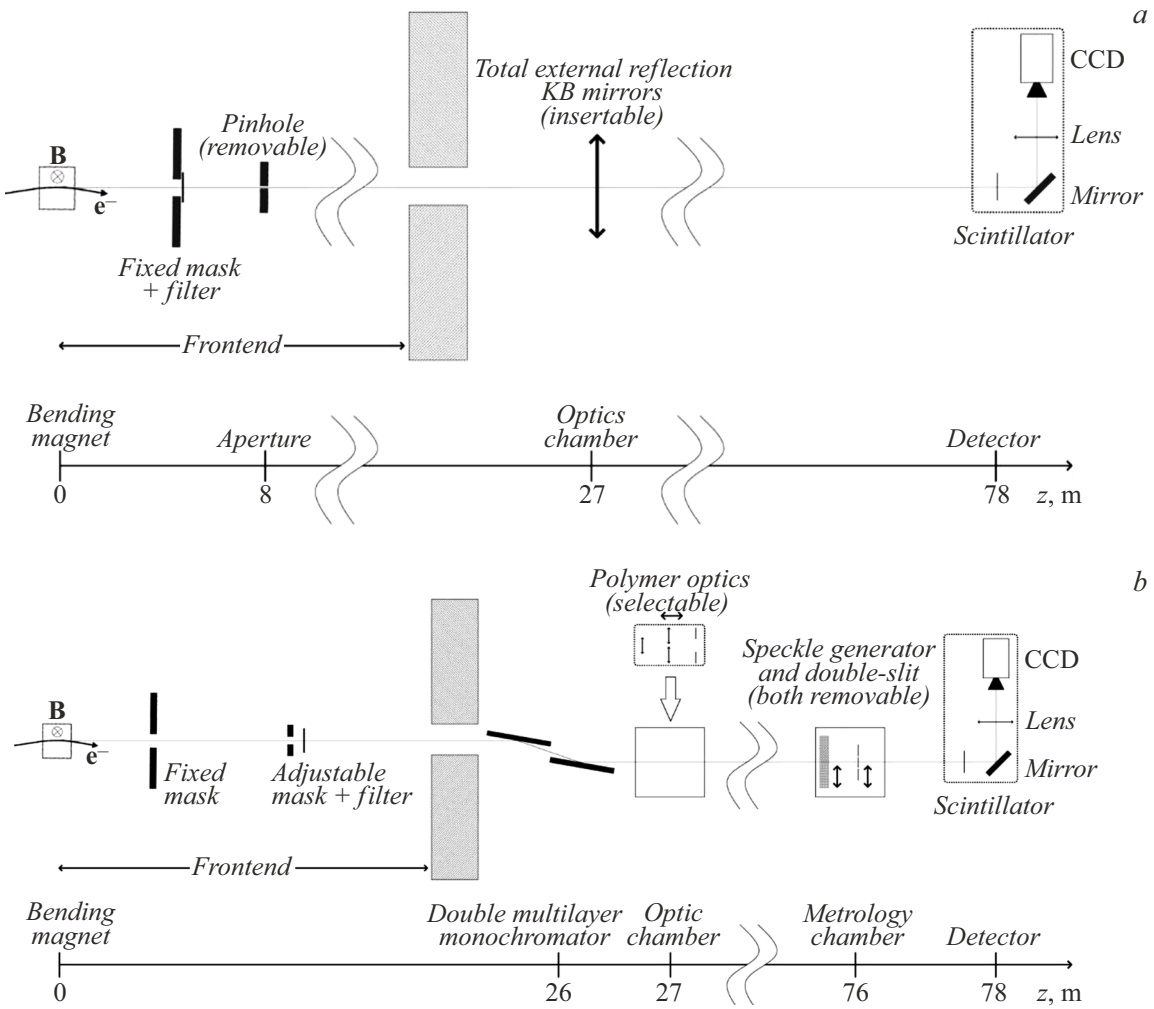

Figure 1. Electron beam emittance measurement setup at the SRF „SKIF“: *a* — at the „X-Ray Beam Diagnostics“ beamline, *b* — at the „Hard X-Ray Metrology“ beamline.

The „Hard X-ray Metrology“ beamline designed for qualification of the X-ray optics at the SRF „SKIF“ also may be used to solve the problems of precision beam emittance measurement and to study the electron beam profile in real time at $E_{ph} \sim 10\,\text{keV}$ using double-mirror multilayer or channel-cut crystal monochromators. The following beam diagnostic modes will be available at the metrology beamline: a camera based on crossed polymer compound refractive lenses (CRL), Young interferometer, Billet interferometer, and heterodyne interferometer. In relevant modes, optical components will be inserted into the SR beam downstream of the monochromators: crossed CRL and Billet split lens placed 27 m from the source, sets of pair slits and a speckle generator — upstream of a 2D detector that is identical to the above-mentioned one and is placed at the experimental room end.

Altogether, the following optical configurations are proposed for hard X-ray beam emittance measurements at the SRF „SKIF“:

1) camera obscura,
2) KB TER mirrors camera,
3) crossed polymer lens camera,
4) Young interferometers — vertical and horizontal;
5) Billet interferometers — vertical and horizontal;
6) heterodyne interferometer.

Cross-validation of beam emittance measurements carried out using various techniques employing different optics will eliminate the effect of individual X-ray optical components.

3. Simulation

The following parameters of the SRF „SKIF“ storage ring were taken for evaluations described below [1]: electron energy $E = 3\,\text{GeV}$, energy spread $\sigma_E/E = 0.0011$, beam current 400 mA, emittances $\varepsilon_{e,x} = 75\,\text{pm·rad}$ and $\varepsilon_{e,y} = 7.5\,\text{pm·rad}$, betatron functions $\beta_x = 0.252\,\text{m}$ and $\beta_y = 7.77\,\text{m}$, dispersion function $\eta_x = 0.003\,\text{m}$. Corresponding beam cross-section dimensions $\sigma_{e,x} = 5.46\,\mu\text{m}$, $\sigma_{e,y} = 7.63\,\mu\text{m}$. Spectrum of SR generated by the electron

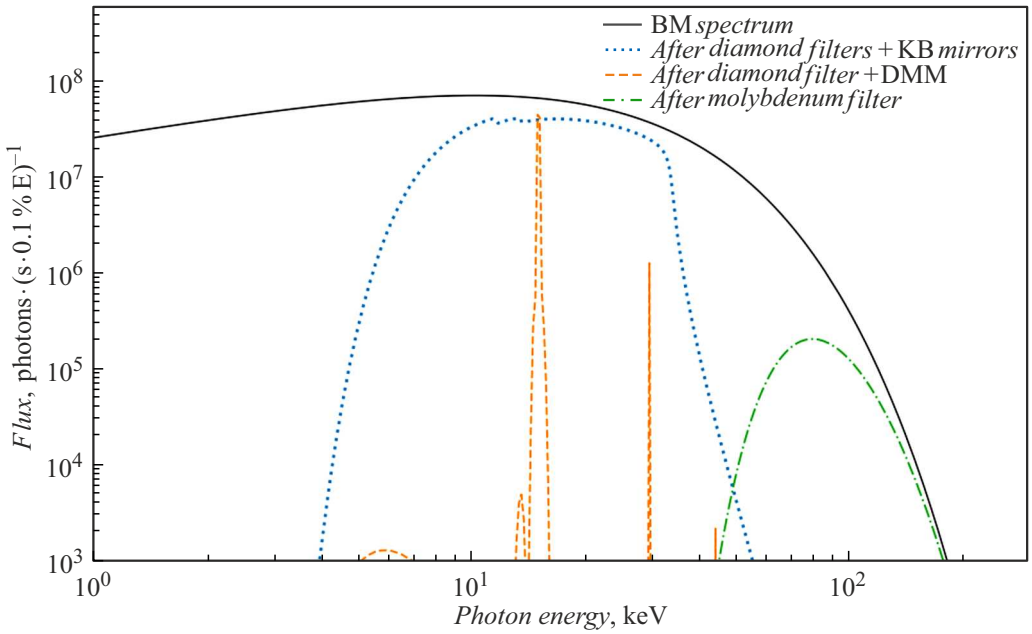

Figure 2. Spectrum of SR emitted into a solid angle of $1\,\mu\text{rad}^2$. A 0.8 mm thick diamond filter is used when imaging a source by achromatic KB mirrors, as well as when using lenses and interferometers with a monochromator. A 1 mm molybdenum filter is used in the camera obscura.

beam in the bending magnet was calculated in Spectra [32] and is shown in Figure 2.

In the camera obscura mode, the 1 mm Mo filter and natural intensity drop in the high photon energy region provide a dome-shaped SR spectrum with its center at $E_{ph} = 80\,\text{keV}$ and FWHM 41 keV. At such high photon energies, the difference of σ_e from σ_{source} may be neglected. PSF for different square pinhole sizes calculated in accordance with (8) at $E_{ph} = 80\,\text{keV}$ are shown in Figure 3. For reasons of balance between the peak width and diffraction „lobe“ size, $A = 14.8\,\mu\text{m}$, corresponding to $\Omega \approx 3.1$, was chosen for further simulation.

PSF for the chosen pinhole at the photon energy of 60, 80 and 100 keV are shown in Figure 4, *a*–*c*, respectively. Spectrum-weighted average PSF after the Mo filter (Figure 2) is shown in Figure 4, *d*. It can be seen that averaging over a broad spectral band smooths down the diffraction „lobes“.

The source image formed by the pinhole on the detector results from the convolution of the ideal $M = q/p = (70\,\text{m})/(8\,\text{m}) = 8.75$-fold magnified source image and spectrum-averaged PSF, Figure 5. Pinhole resolution is $\sigma_{pinhole}/M = 32.3/8.75 \approx 3.7\,\mu\text{m}$. Such high magnification factor weakens the requirements for detector PSF narrowness, making it possible to increase the scintillator thickness, which is important for effective SR detection within $E_{ph} > 30\,\text{keV}$.

When a pair of elliptic cylindrical total external reflection KB mirrors is used as high-light-transmission achromatic imaging optics, diffraction broadening turns out to be negligibly small (compared with the pinhole),

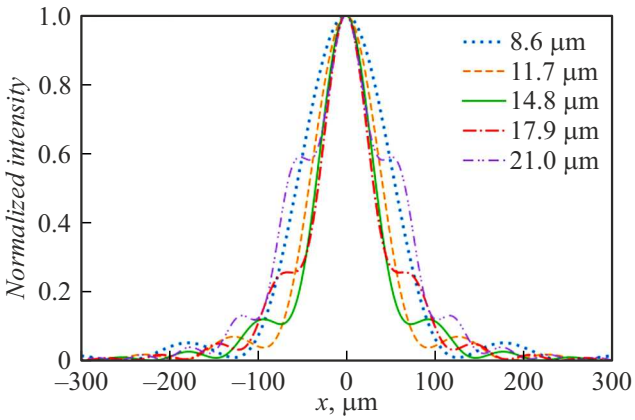

Figure 3. PSF for different pinhole sizes *A*.

however, PSF becomes a coordinate function of the camera field of view. System magnification will be $M \approx 1.89$ ($q/p \approx (51\,\text{m})/(27\,\text{m})$, for the purpose of calculation, the difference in mirror center positions was set to 205 mm). SR spectrum in such camera is formed by the 0.8 mm diamond filter transmission coefficient curve and the Pt mirror coating reflection coefficient curve at a grazing angle of 2.5 mrad (Figure 2). Resulting spectral band is 8–32 keV.

Imaging by the KB mirror system was simulated by raytracing using Shadow 3 [33] included in OASYS package [34]. SR beam caustic near the KB mirrors focus is shown in Figure 6. It can be seen that such imaging system has a large depth of focus or, in other words, low sensitivity to the detector positioning error along the optical axis.

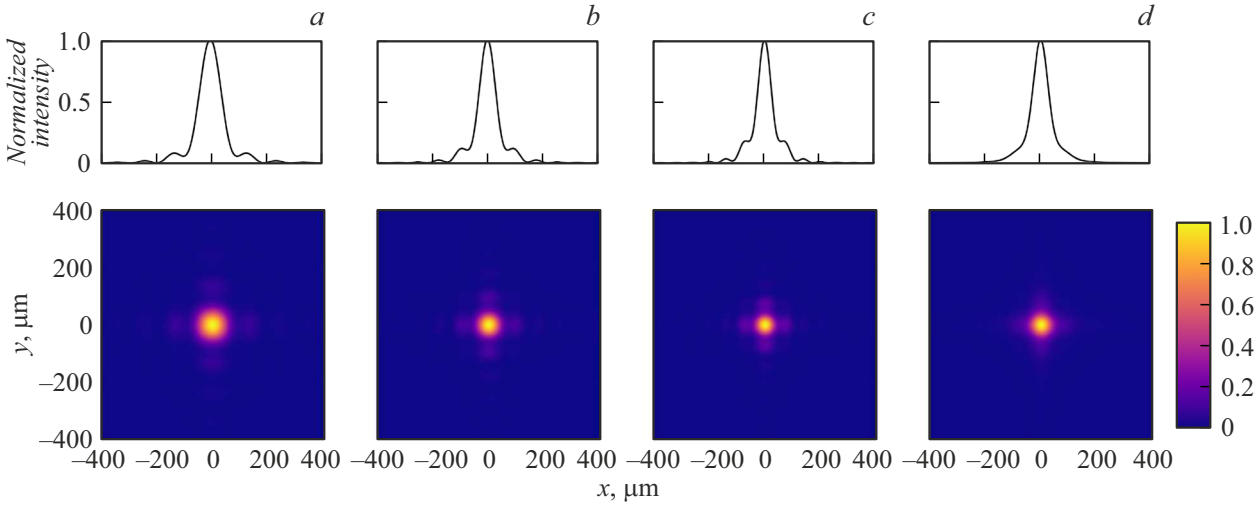

Figure 4. PSF for the pinhole with $A = 14.8\,\mu$m: a — at $E_{ph} = 60$ keV, b — at $E_{ph} = 80$ keV, c — at $E_{ph} = 100$ keV, d — after the molybdenum filter SR-spectrum-averaged PSF. Color scale hereinafter corresponds to the intensity normalized to unity.

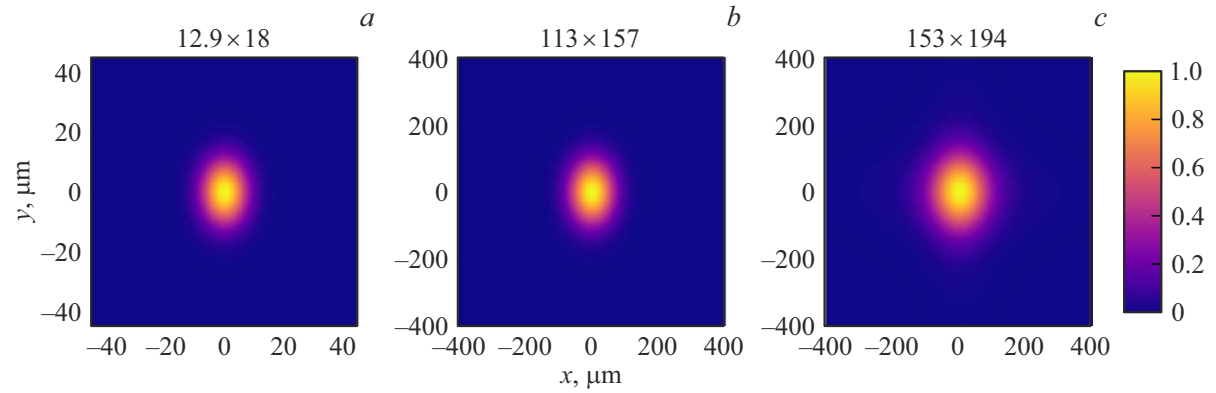

Figure 5. Source (a), ideal magnified source image (b) and pinhole-formed image (c). $2.355 \cdot \sigma$ spot sizes are given in μm.

To consider focal spot blurring due to low-frequency and medium-frequency errors of mirror surfaces, error profiles with rms 1 nm were generated (Figure 7).

Comatic aberration that limits the field of view makes the main contribution to the source image distortion induced by the KB camera. Images formed by the KB system at various transverse shifts of the source, taking into account the mirror surface errors, are shown in Figure 8.

A field of view of 1 mm turns out to be coma-free and is 100 times larger than the source dimensions. In addition, the coma may be partially compensated during further image processing. For direct observation of a source with high time resolution in a wider field of view, a Wolter mirrors camera shall be addressed separately.

Compound refractive lenses may serve as alternative optics for source imaging. Made using the LIGA technology, polymer lenses may be considered as X-ray amorphous [35], while the surface shape errors of such lenses are negligibly small [36,37]. Therefore, the simulation used SU-8 polymer cylindrical parabolic lenses with crossed configuration, apical curvature radius of 0.5 mm and aperture of $A = 1.4$ mm,

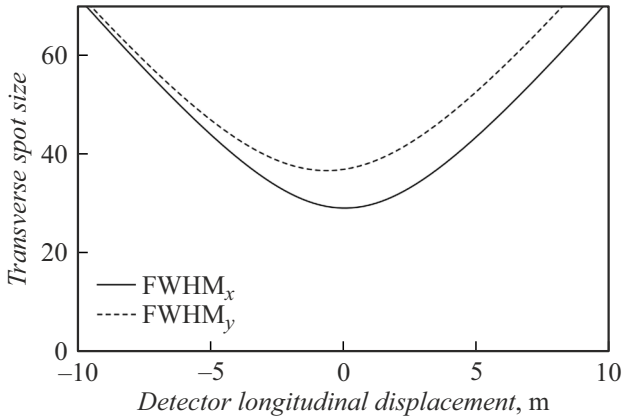

Figure 6. FWHM cross-section dimensions of the SR beam near the KB mirror system focus.

which was inherently larger than the transverse coherence lengths of the SR beam at $p = 27$ m and $E_{ph} = 18.4$ keV. Magnification $M = q/p \approx 1.89$.

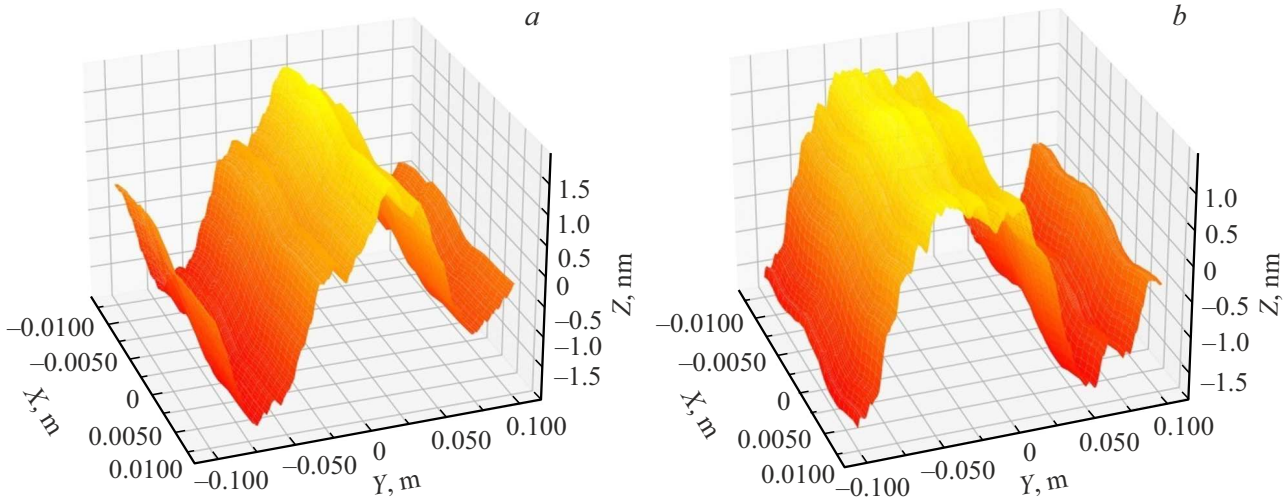

Figure 7. Generated KB system error profiles used for the calculations: *a* — for a horizontally focusing mirror, *b* — for a vertically focusing mirror. The *X* axis is oriented across the SR beam, the *Y* axis is oriented along the SR beam.

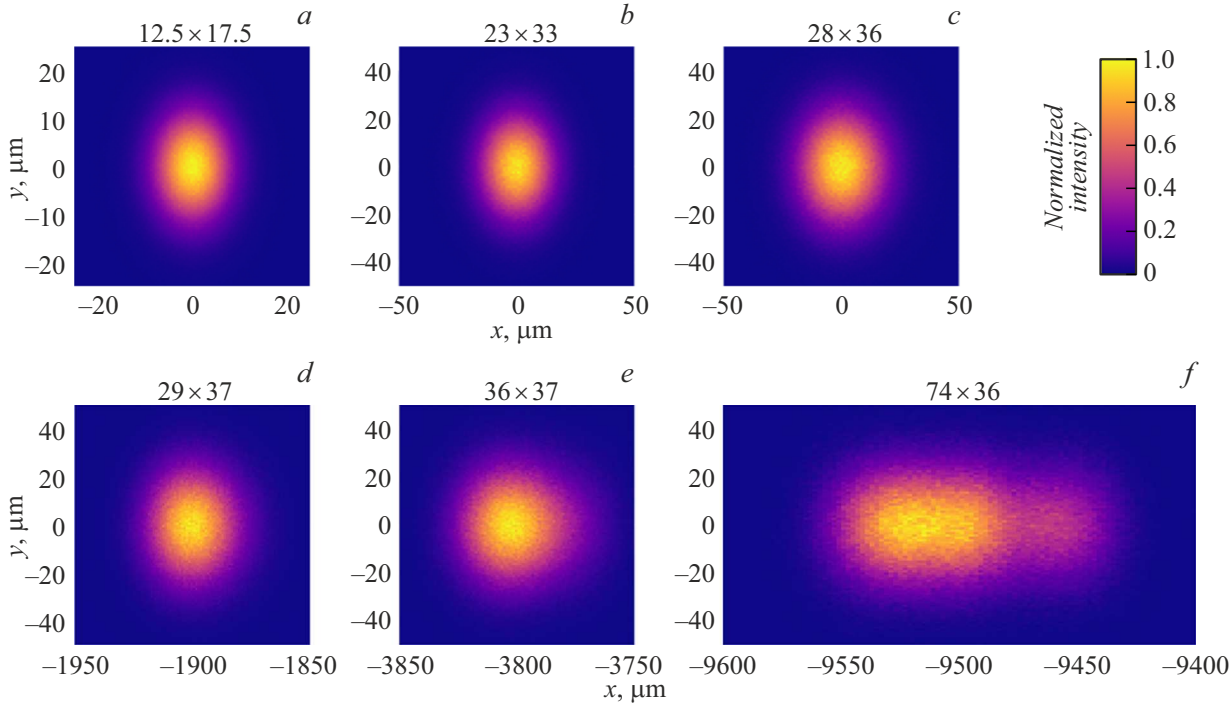

Figure 8. Raytracing results: *a* — source; *b* — magnified source image produced by the ideal KB mirrors; *c* — image produced by the KB mirrors with error profiles; *d*–*f* — images produced by the KB mirrors with error profiles with a horizontal shift of the source by 1, 2 and 5 mm, respectively. FWHM spot sizes are given in μm.

X-ray refractive lenses have a pronounced coordinate chromatism and, therefore, require SR monochromatization. For source imaging, chromatic aberrations are significant even when a double-mirror multilayer monochromator with the bandwidth $\Delta E_{ph}/E_{ph} \sim 10^{-2}$ is used, Figure 9, *b*. Nevertheless, when using the channel-cut crystal monochromator with $\Delta E_{ph}/E_{ph} \sim 10^{-4}$, such lenses can produce an aberration-free image in a large field of view (Figure 9, *c, d*). For the purpose of electron beam observation in the storage ring of the SRF „SKIF“ the field of view of lenses may be considered as unlimited. On the other hand, the camera based on a channel-cut monochromator and refractive lenses is four orders of magnitude behind the KB mirror camera in terms of the light transmission, which limits its employment for measurements with high time resolution.

Note also that refractive lenses may easily serve as a compound microscope (with lens and eyepiece) with a

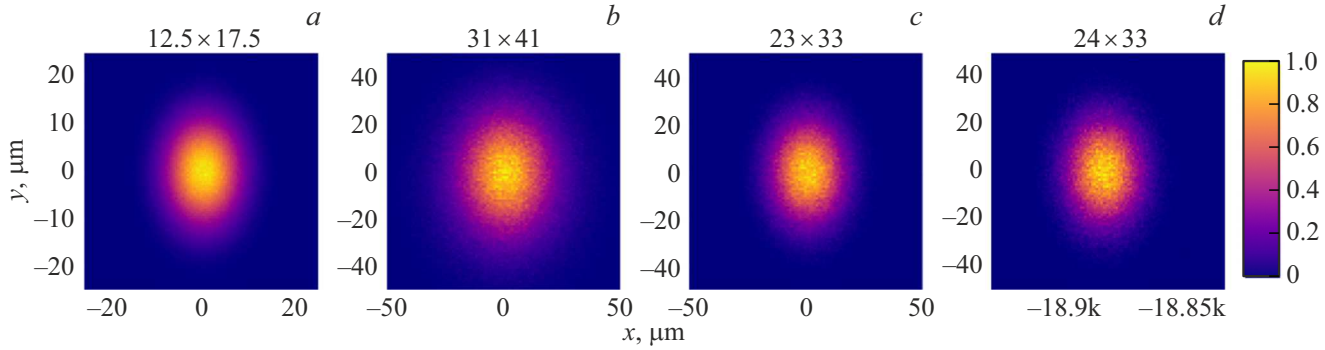

Figure 9. Raytracing results: *a* — source; *b* — magnified source image produced by lenses using the double-mirror monochromator with Mo/B_4C coating [38]; *c, d* — images produced by lenses using the channel-cut Si(111) monochromator with a horizontal shift of the source by 0 mm and 10 mm, respectively. FWHM spot sizes are given in μm.

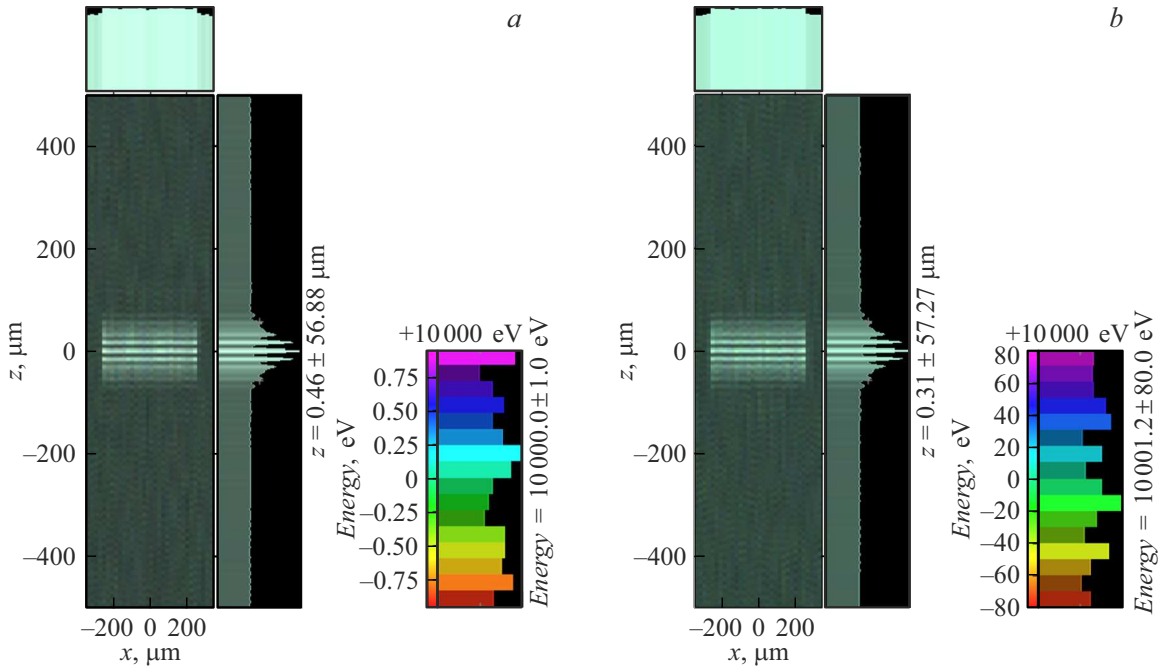

Figure 10. Young's hard X-ray double-slit experiment simulation, E_{ph} = 10 keV: *a* — for monochromatic radiation downstream of the channel-cut Si(111) monochromator, *b* — for „pink“ radiation downstream of the Mo/B_4C multilayer monochromator. Radiation quantum energy is marked with color, relative intensity is marked with brightness. Slit center-to-center distance is 50 μm, slit width is 10 μm.

higher magnification factor for observation of an electron beam, reducing the detector PSF narrowness requirements.

To demonstrate hard X-ray interferometry applicability for beam diagnostics at the SRF „SKIF“ Young's experiment was simulated The calculation was performed by adding up the intensities of radiation emitted by Gaussian-distributed „macroelectrons“ in accordance with the expected dimensions and electron beam divergence in a strong-field bending magnet. The calculation was performed in XRT [39]. Channel-cut Si(111) monochromator and Mo/B_4C double-mirror multilayer monochromator applications were addressed. Examples of interference patterns in the detector plane are shown in Figure 10. The calculation indicates that the double-mirror monochromator is sufficient, i.e. interferometric measurements on the „pink“ beam are possible.

Conclusion

Characterization of an electron beam on synchrotron radiation sources is necessary both for the storage ring feedback system operation and for X-ray optics metrology and microscopy tasks. The study proposed a hard X-ray beam emittance measurement program at the SRF „SKIF“. In particular, a concept of the „X-ray Beam Diagnostics“ beamline designed for continuous electron beam monitoring through source imaging by a camera obscura or high-light-transmission total external reflection imaging mirror

optics in polychromatic radiation conditions was proposed. Moreover, it was proposed to use additional source imaging through a compound refractive lens and to employ complementary hard X-ray interferometric techniques in monochromatic radiation conditions at the „Hard X-Ray Metrology“ beamline.

In the most conservative measurement setup, i.e. using the camera obscura, the expected resolution is $3.7\,\mu$m.

Funding

This work was performed within the framework of a budget project of the Ministry of Science and Higher Education of the Russian Federation for Synchrotron radiation facility SKIF, Boreskov Institute of Catalysis (FWUR-2024-0042).

Conflict of interest

The authors declare no conflict of interest.

References

[1] G. Baranov, A. Bogomyagkov, I. Morozov, S. Sinyatkin, E. Levichev. Phys. Rev. Accel. Beams, **24** (12), 120704 (2021). DOI: 10.1103/PhysRevAccelBeams.24.120704
[2] P. Willmott. *An introduction to synchrotron radiation: techniques and applications* (John Wiley & Sons, 2019), DOI: 10.1002/9781119280453
[3] C. Thomas, G. Rehm, I. Martin, R. Bartolini. Phys. Rev. Spec. Top. Accel. Beams, **13** (2), 022805 (2010). DOI: 10.1103/PhysRevSTAB.13.022805
[4] P. Elleaume, C. Fortgang, C. Penel, E. Tarazona. J. Synchrotron Radiat., **2** (5), 209 (1995). DOI: 10.1107/S0909049595008685
[5] H. Sakai, M. Fujisawa, K. Iida, I. Ito, H. Kudo, N. Nakamura, K. Shinoe, T. Tanaka. Phys. Rev. Spec. Top. Accel. Beams, **10** (4), 042801 (2007). DOI: 10.1103/PhysRevSTAB.10.042801
[6] T. Weitkamp, O. Chubar, M. Drakopoulos, A. Souvorov, I. Snigireva, A. Snigirev, F. Günzler, C. Schroer, B. Lengeler. Nucl. Instrum. Methods Phys. Res. A, **467**, 248 (2001). DOI: 10.1016/S0168-9002(01)00284-4
[7] T.R. Renner, H.A. Padmore, R. Keller. Rev. Sci. Instrum., **67** (9), 3368 (1996). DOI: 10.1063/1.1147369
[8] D.C. Zhu, J.H. Yue, Y.F. Sui, D.H. Ji, J.S. Cao, K.R. Ye, S.Q. Tian, J. Chen, Y.B. Leng. Nucl. Sci. Tech., **29**, 148.1 (2018). DOI: 10.1007/s41365-018-0477-y
[9] V. Nazmov, M. Kluge, A. Last, F. Marschall, J. Mohr, H. Vogt, R. Simon. Microsyst. Technol., **20** (10), 2031 (2014). DOI: 10.1007/s00542-013-2056-9
[10] W. Leitenberger, H. Wendrock, L. Bischoff, T. Weitkamp. J. Synchrotron Radiat., **11** (2), 190 (2005). DOI: 10.1107/S0909049503029169
[11] L. Assoufid, X. Shi, S. Marathe, E. Benda, M.J. Wojcik, K. Lang, R. Xu, W. Liu, A.T. Macrander, J.Z. Tischler. Rev. Sci. Instrum., **87** (5), 052004 (2016). DOI: 10.1063/1.4950775
[12] Y. Kashyap, H. Wang, K. Sawhney. Phys. Rev. A, **92** (3), 033842 (2015). DOI: 10.1103/PhysRevA.92.033842
[13] M. Siano, B. Paroli, M.A.C. Potenza, L. Teruzzi. Phys. Rev. Accel. Beams, **25** (5), 052801 (2022). DOI: 10.1103/PhysRevAccelBeams.25.052801
[14] J. Breunlin, Å. Andersson, N. Milas, Á. Saá Hernández, V. Schlott. Nucl. Instrum. Methods Phys. Res. A, **803**, 55 (2015). DOI: 10.1016/j.nima.2015.09.032
[15] E.J. Jaeschke, S. Khan, J.R. Schneider, J.B. Hastings. *Synchrotron Light Sources and Free-Electron Lasers* (Springer, 2020). DOI: 10.1007/978-3-030-23201-6
[16] P.F. Tavares, S.C. Leemann, M. Sjöström, Å. Andersson. J. Synchrotron Radiat., **21** (5), 862 (2014). DOI: 10.1107/S1600577514011503
[17] L. Liu, N. Milas, A.H. Mukai, X.R. Resende, F.H. de Sá. J. Synchrotron Radiat., **21** (5), 904 (2014). DOI: 10.1107/S1600577514011928
[18] G. Kube. Proc. DIPAC, **35**, 6 (2007).
[19] A. Trebushinin, G. Geloni, Y. Rakshun, S. Serkez. Optica, **9** (8), 842 (2022). DOI: 10.1364/OPTICA.460902
[20] A. Trebushinin, G. Geloni, S. Serkez, R. Khubbutdinov, E. Saldin. Phys. Rev. Accel. Beams, **27** (3), 032802 (2024). DOI: 10.1103/PhysRevAccelBeams.27.032802
[21] G. Geloni, E. Saldin, E. Schneidmiller, M. Yurkov. *Statistical optics approach to the design of beamlines for synchrotron radiation* (2006), arXiv preprint physics/0603269
[22] N. Samadi, X. Shi, L. Dallin, D. Chapman. Phys. Rev. Accel. Beams, **23** (2), 024801 (2020). DOI: 10.1103/PhysRevAccelBeams.23.024801
[23] V.P. Nazmov, E.F. Reznikova, A. Somogyi, Ju. Mohr, V. Saile. Proc. SPIE, **5539**, 235 (2004). DOI: 10.1117/12.562615
[24] V. Nazmov, E. Reznikova, A. Last, J. Mohr, V. Saile, M. DiMichiel, J. Göttert. Nucl. Instrum. Methods Phys. Res. A, **582** (1), 120 (2007). DOI: 10.1016/j.nima.2007.08.076
[25] E. Pestov, A.K. Chernyshev, M.S. Mikhailenko, M.V. Zorina, E.I. Glushkov, E.V. Petrakov, I.V. Malyshev, N.I. Chkhalo, D.G. Reunov. Appl. Opt., **64** (4), 837 (2025). DOI: 10.1364/AO.542363
[26] A. Snigirev, I. Snigireva, V. Kohn, V. Yunkin, S. Kuznetsov, M.B. Grigoriev, T. Roth, G. Vaughan, C. Detlefs. Phys. Rev. Lett., **103** (6), 064801 (2009). DOI: 10.1103/PhysRevLett.103.064801
[27] O.V. Chubar. IEEE Proc. Part. Accel. Conf., **4**, 2447 (1995). DOI: 10.1109/PAC.1995.505579
[28] M. Born, E. Wolf. *Principles of Optics*, 7th ed. (Cambridge University Press, 1999)
[29] T. Naito, T. Mitsuhashi. Phys. Rev. ST Accel. Beams, **9** (12), 122802 (2006). DOI: 10.1103/PhysRevSTAB.9.122802
[30] K.S. Morgan, D.M. Paganin, K.K.W. Siu. Appl. Phys. Lett., **100** (12), 124102 (2012). DOI: 10.1063/1.3694918
[31] R. Cerbino, L. Peverini, M.A.C. Potenza, A. Robert, P. Bösecke, M. Giglio. Nat. Phys., **4** (3), 238 (2008). DOI: 10.1038/nphys837
[32] T. Tanaka. J. Synchrotron Radiat., **28** (4), 1267 (2021). DOI: 10.1107/S1600577521004100
[33] M.S.D. Rio, N. Canestrari, F. Jiang, F. Cerrina. J. Synchrotron Radiat., **18** (5), 708 (2011). DOI: 10.1107/S0909049511026306
[34] M.S.D. Rio, L. Rebuffi. AIP Conf. Proc., **2054** (1), 060081 (2019). DOI: 10.1063/1.5084712
[35] V. Nazmov, E. Reznikova, J. Mohr, V. Saile, L. Vincze, B. Vekemans, S. Bohic, A. Somogyi. J. Micromech. Microeng., **21** (1), 015020 (2010). DOI: 10.1088/0960-1317/21/1/015020
[36] V. Nazmov, E. Reznikova, J. Mohr, A. Snigirev, I. Snigireva, S. Achenbach, V. Saile. Microsyst. Technol., **10**, 716 (2004). DOI: 10.1007/s00542-004-0433-0
[37] M. Simon, E. Reznikova, V. Nazmov, A. Last. Microsyst. Technol., **14** (9–11), 1727 (2008). DOI: 10.1007/s00542-008-0618-z

[38] E.I. Glushkov, A.A. Akhsakhalyan, P.A. Veprev, I.G. Zabrodin, M.V. Zorina, I.V. Malyshev, M.S. Mikhailenko, A.E. Pestov, E.V. Petrakov, R.S. Pleshkov, V.N. Polkovnikov, D.G. Reunov, A.B. Ulasevich, A.K. Chernyshov, N.I. Chkhalo, R.A. Shaposhnikov, Ya.V. Rakshun, Yu.V. Khomyakov, V.A. Chernov. ZhTF, (in Russian) **95** (10), (2025).
[39] K. Klementiev, R. Chernikov. Proc. SPIE, **9209**, 60 (2014). DOI: 10.1117/12.2061400

Translated by E.Ilinskaya

Translated by E.Ilinskaya